Electronic Supplementary Material (ESI) for Chemical Communications.

Inorganic co-crystal formation and thermal disproportionation in a dicyanometallate "superperovskite"

SUPPLEMENTARY INFORMATION

Joshua A. Hill,[a,b] Claire A. Murray,[c] Chiu C. Tang,[c] Peter M. M. Thygesen,[a]
Amber L. Thompson,[a] and Andrew L. Goodwin[a*]

[a]Department of Chemistry, University of Oxford, Inorganic Chemistry Laboratory,
South Parks Road, Oxford OX1 3QR, U.K.
[b]Conservation of Wall Painting Department, Courtauld Institute of Art, Somerset House,
Strand, London WC2R 0RN, UK
[c]Diamond Light Source Ltd., Harwell Science and Innovation Campus,
Didcot, Oxfordshire OX11 0DE, UK
*To whom correspondence should be addressed; E-mail: andrew.goodwin@chem.ox.ac.uk.

Submitted to Chem. Commun.

Contents

Supplementary information reproduced with modifications from Hill[S1].

1 Synthesis

A typical small-scale synthesis of $Bu_4N]Mn[Au(CN)_2]_3 \cdot [Bu_4N]ClO_4$ (**1**) was as follows. Moderately sized single crystals formed overnight from a concentrated ethanolic mixture of $[Bu_4N]Au(CN)_2 \cdot \frac{1}{2}H_2O$ (28 mg in 0.25 mL ethanol) and $MnClO_4 \cdot xH_2O$ (13 mg in 0.20 mL ethanol) solutions. Crystals were isolated by filtration, washed with ethanol, and dried under vacuum before being ground to a fine white powder. Syntheses of powder samples followed a similar procedure on an increased scale. (**1**) was first formed fortuitously in attempts to make a Mn analogue of the **bcs**-structured $[Bu_4N]Ni[Au(CN)_2]_3$.

Elemental Analysis

The formula of (**1**) is consistent with elemental analysis found (calculated) % C 32.68 (32.92); H 5.12 (5.23); N 7.90 (8.08); Cl 2.55 (2.56). Elemental analysis was carried out by MEDAC Ltd.

2 Single-crystal X-ray diffraction

Methods

In-house single-crystal X-ray diffraction data were collected using an Oxford Diffraction (Rigaku Oxford Diffraction) SuperNova diffractometer fitted with an Oxford Cryosystems Cryostream 700 Plus open-flow nitrogen cooling device.[S2] All crystals were coated in perfluorpolyether oil and mounted on a MiTeGen loop. CrysAlisPro[S3] was used for data collection and reduction.

Data at 30 K were collected at Diamond Light Source (beamline I19)[S4] ($\lambda = 0.6889\,\text{Å}$) fitted with an Oxford Cryosystems HeliX open-flow helium cryostat,[S5] and Rigaku Saturn 724+ CCD detector. CrystalClear and CrysAlisPro[S3] were used for data collection and reduction respectfully.

Structural refinement was carried out with full-matrix least-squares on F or F^2 using CRYSTALS.[S6, S7] Hydrogen atoms were, in some cases, visible in the difference Fourier map and treated in the usual manner.[S8] In the remaining cases, and particularly for disordered assemblies, hydrogen atoms were added geometrically.

Discussion

Pertinent details of the single crystal diffraction data are summarised here along with an account of the development of the crystallographic model. Crystallographic details of synchrotron single-crystal diffraction at 30 K are given in Table S1.

The essentially cubic $\{\text{Mn[Au(CN)}_2]_3\}^-$ framework accounts for 51 % of the electron density in $[\text{Bu}_4\text{N}]\text{Mn[Au(CN)}_2]_3\cdot[\text{Bu}_4\text{N}]\text{ClO}_4$ and therefore dominates the scattering. However, it is readily apparent from reciprocal-space reconstructions that this system cannot be cubic due to characteristic diffuse scattering in only one set of pseudo-cubic planes [Figure S1(b)]. This means the model should be in a tetragonal or lower crystal system.

Table S1: Crystallographic details of [Bu$_4$N]Mn[Au(CN)$_2$]$_3$·[Bu$_4$N]ClO$_4$ derived from synchrotron single-crystal diffraction at 30 K.

Compound	[Bu$_4$N]Mn[Au(CN)$_2$]$_3$·[Bu$_4$N]ClO$_4$ (**1**)
Empirical formula	Mn$_1$Au$_3$C$_{38}$N$_8$H$_{72}$Cl$_1$O$_4$
Formula weight (g mol^{-1})	1386.32
Crystal System	Tetragonal
Space Group	$P4/ncc$ (No. 130) Origin Choice 2
Z	8
Radiation (Å)	$\lambda = 0.68890$
Crystal colour	Colourless
Crystal size (mm)	$0.01\times0.01\times0.01$
Temperature (K)	30(0.5)
a (Å)	21.4048(3)
c (Å)	21.3901(2)
V (Å^3)	9800.2(2)
μ (mm^{-1})	8.538
Reflections ($I > 2\sigma(I)$)	5488
R (F_o)	0.1286
R$_w$ (F_o)	19.23
GOF	1.0653
Minimisation	F

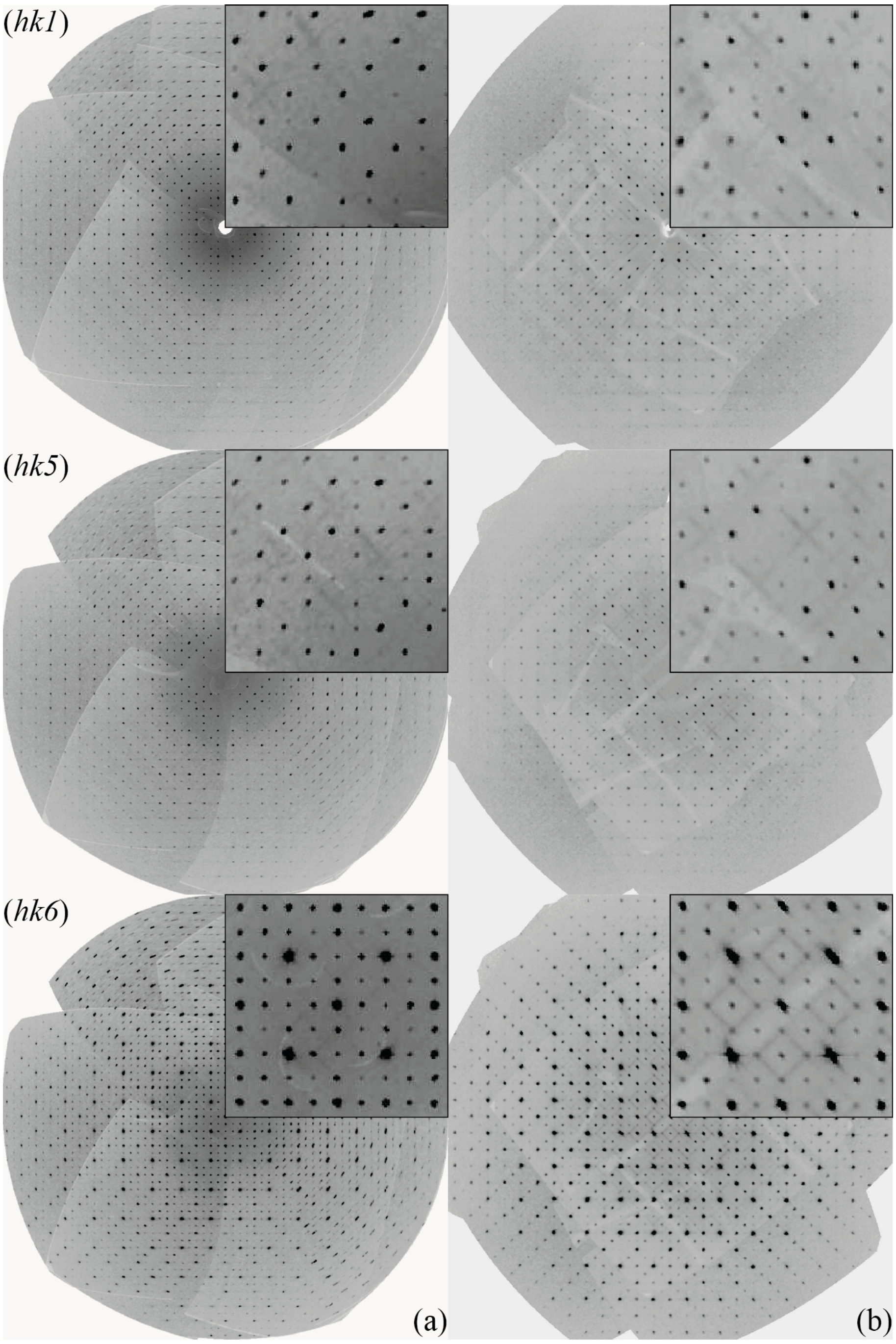

Figure S1: Reciprocal space reconstructions of the $(hk1)$, $(hk5)$, and $(hk6)$ planes for data collected at 30 K on beamline I19 using $\lambda = 0.6889\,\text{Å}$ (a) and at 298(1) K in-house using $\text{Cu}_{\text{K}_\alpha}$ (b). The diffuse scattering is substantially reduced at low temperature.

The structural model was built up gradually in both size and complexity starting from the basic perovskite structure. Since the majority of the scattering comes from the framework, the most intense peaks can be indexed on a $\sim 10 \times 10 \times 10\,\text{Å}$ unit cell in $P4/mmm$ which corresponds to one perovskite cube. This ignores the weaker peaks which give a $\sim 20 \times 20 \times 20\,\text{Å}$ unit cell. After this initial insight from working with in-house data it was decided that to collect data at the I19 instrument (Diamond Light Source) at a temperature of 30 K to potentially help reduce the apparent correlated disorder in the compound.

Building up from the $\sim 10 \times 10 \times 10\,\text{Å}$ model in $P4/mmm$ the corresponding $\sim 20 \times 20 \times 20\,\text{Å}$ (*i.e.* $2 \times 2 \times 2$ perovskite) cell should be in the maximal subgroup $I4/mcm$. As the body-centre violations in this system are fairly weak this seemed a reasonable next step. The residual electron density was, however, still very disordered indicating that the body centring should be removed. Dropping the symmetry to $P4/ncc$, which gave the highest R_{int} value of all the maximal subgroups of $I4/mcm$, allowed further progress to be made. The crucial step in coming to the final model was in recognising that both of the extra-framework species are incompatible with high symmetry sites. In this space group it cannot be avoided putting one or the other on, or near, sites with symmetries of 2.22 and 4. By using the second origin choice of $P4/ncc$ it was possible to move $[\text{Bu}_4\text{N}]^+$ onto a low symmetry site to give only one, ordered equivalent in the asymmetric unit. This results in there being two $[\text{ClO}_4]^-$ units in the asymmetric unit which are centred on or near the $4a$ (2.22 symmetry) and $4c$ (4..) Wyckoff sites. It is important to note that the final Wyckoff positions of the Cl of the $[\text{ClO}_4]^-$ in the single crystal model are actually $16g$ and $4c$. The latter symmetry is clearly incompatible with the tetrahedral molecular symmetry of perchlorate. While it may be preferable to lower the symmetry to relieve the inevitable disorder across these symmetry elements, the packing of $[\text{Bu}_4\text{N}]^+$ suggests that it may be reasonable, or indeed necessary, for the perchlorate ions to be disordered. In this solution the $[\text{Bu}_4\text{N}]^+$ pack to give two different pseudo-octahedral cavities [Figure S2] meaning that the system must accommodate a tetrahedral species within an octahedral hole.

The residual electron density around the perchlorate sites (the centres of the pseudocubic perovskite cubes) looks, necessarily, rather octahedral [Figure S3(a,b)]. Examination of this residual density led to the construction of a disorder model based on three tetrahedra, each with one oxygen pointing toward the symmetry inequivalent arms of the residual density. Each tetrahedron should then be free to 'rotate' around this Cl—O bond giving a torus of electron density instead of 3 resolved oxygen atoms. The residual density of 377 (392 ideal) electrons per unit cell when no perchlorate is included as found by PLATON SQUEEZE is consistent with the presence of 8 perchlorate anions per unit cell.[S9, S10] Inclusion of the disordered perchlorate (without implementing the tori) within the pseudo-octahedral sites [Figure S3(c,d)] gives the structural model in Figure S3(e) for which crystallographic details are summarised in Table S1.

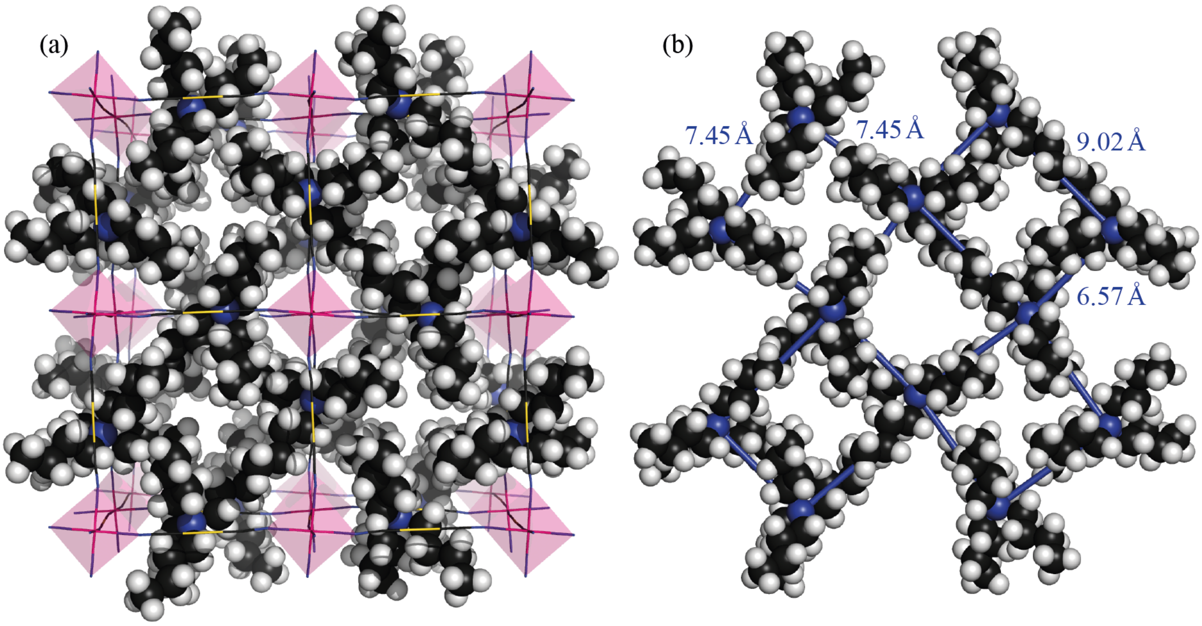

Figure S2: (a) In $[Bu_4N]Mn[Au(CN)_2]_3 \cdot [Bu_4N]ClO_4$ ($[ClO_4]^-$ not shown) the packing of $[Bu_4N]^+$ centred on the ac and bc faces gives two different pseudo-octahedral holes by interdigitation in the ab plane. The same holes lie above each other along c (b) The geometry of the squares formed by linking the centres of the cations indicating the N$\cdots$N distances.

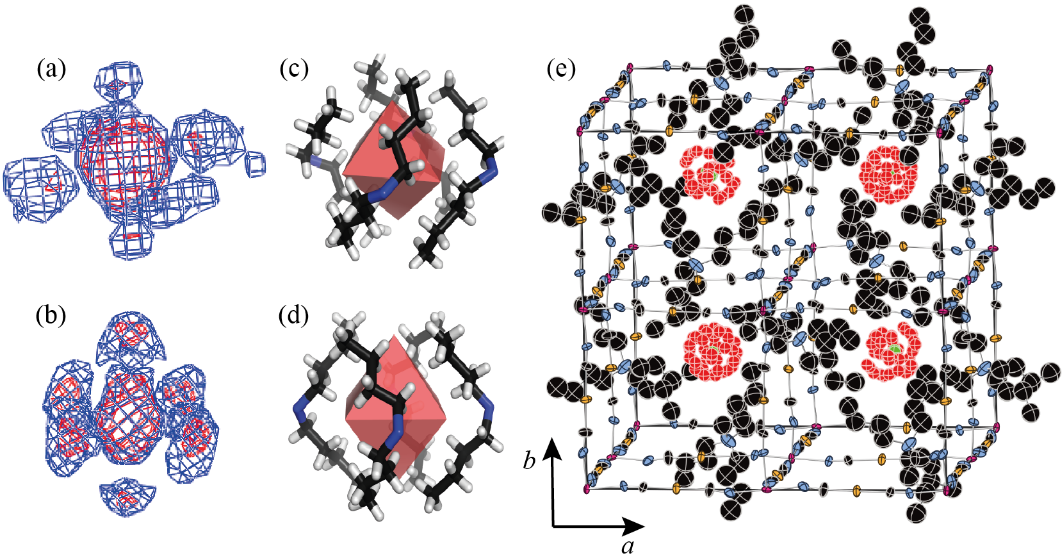

Figure S3: The residual density around the a (a) and c (b) Wyckoff sites. Due to the high site symmetry the residual density looks close to octahedral. Large, non-spherical density at the centre of the 'octahedra' is probably indicative of perchlorate off-centring. Pseudo-octahedral sites shown with red polyhedra at the $4a$ (c) and $4c$ (d) Wyckoff sites. A full structure solution including a disordered perchlorate (e). Only half of the extra-framework ions are shown and no hydrogen atoms are shown for clarity. Manganese in pink, gold in yellow, nitrogen in blue, carbon in black, oxygen in red, and chlorine in green.

3 Powder diffraction

Methods

In-house powder diffraction patterns were collected using a PANalytical Empyrean diffractometer equipped with $\text{Cu}_{\text{K}_{\alpha_1}}$ radiation ($\lambda = 1.54056\,\text{Å}$) fitted with a Ge(111) monochromator in Bragg-Brentano geometry. Soller slits of 0.04 rad were used in all cases along with a PIXcel 1D detector. A steel spinner sample holder was used of 10 mm diameter. In these cases, variable divergence slits with a fixed sample illumination of 10 mm was used.

Variable temperature powder diffraction data were collected at Beamline I11, Diamond Light Source. Powders were finely ground and loaded into 0.5 mm borosilicate glass capillaries, which were then mounted on specially made brass pins. Data were collected between 140 and 480 K every 10 K using an Oxford Cryosystems cryostream ramping at 360 K hr^{-1} and oriented parallel to the capillary.[S2] Each temperature point was allowed to stabilise before exposure rather than collecting while ramping. The nominal temperature for each collection was outputted to a log file and no internal temperature standard was used. A wavelength of 1.078265(10) Å (roughly 11.5 keV) was used for all samples.[1] Data were collected using the I11 position sensitive detector (PSD): a time-resolved detector which is comprised of a number of Mythen2 detector modules. A collection time of 2 s was used, with the resulting data being the sum of two collections offset by 0.25 ° in 2θ. This is necessary as the detector is made up of discrete modules with small gaps between these units.

Pawley and Rietveld analyses were carried out using non-linear least squares refinement as implemented in TOPAS Academic V4.1.[S11] In general, a TCHZ peakshape was used. For synchrotron data, the peakshape parameters, along with the zero offset were refined from a Si standard collected at room temperature. Peak shape parameters were refined for one temperature and subsequently fixed. Lorentzian and Gaussian strain parameters were used to account for sample-specific contributions to peakshape. Riteveld refinements were based on (analogous) structures determined from single crystal diffraction with a limited number of parameters refined as discussed in the main text.[S12–15]

Discussion

Variable temperature powder diffraction data in Figure S4 show two distinct regions of the diffraction data with an irreversible phase transition occurring at 380 K.

The powder diffraction up to 380 K is consistent with the single crystal structure of $[\text{Bu}_4\text{N}]\text{Mn}[\text{Au(CN)}_2]_3\cdot[\text{Bu}_4\text{N}]\text{ClO}_4$. A typical Pawley refinement fit is shown in Figure S5(a). Coefficients of thermal expansion for $[\text{Bu}_4\text{N}]\text{Mn}[\text{Au(CN)}_2]_3\cdot[\text{Bu}_4\text{N}]\text{ClO}_4$ in the range 140–380 K were found to be $\alpha_a = 23.97(9)$ MK^{-1}, $\alpha_c = 24.65(8)$ MK^{-1}, and $\alpha_V = 73.0(2)$ MK^{-1}[Figure S5(b)]. Refinement results are detailed in Table S2.

At 380 K $[\text{Bu}_4\text{N}]\text{Mn}[\text{Au(CN)}_2]_3\cdot[\text{Bu}_4\text{N}]\text{ClO}_4$ transforms into a different high-symmetry phase. The powder diffraction is very similar to the 6-connected structure with **bcs** topology as reported for $[\text{Bu}_4\text{N}]\text{Ni}[\text{Au(CN)}_2]_3$ [Figure S6(a)].[S12] This compound, as determined from single-crystal data, was reported in space group $I4_1cd$. The Mn-analogue phase here, **bcs**-$[\text{Bu}_4\text{N}]\text{Mn}[\text{Au(CN)}_2]_3$ (**2**), first appears at 380 K and the starting phase is absent after 410 K.

---

[1] The normal operational energy for I11 is 15 keV but this wavelength could not be used due to its proximity to the gold L I 2s, L II 2p 1/2, and L III 2p 3/2 absorption edges.

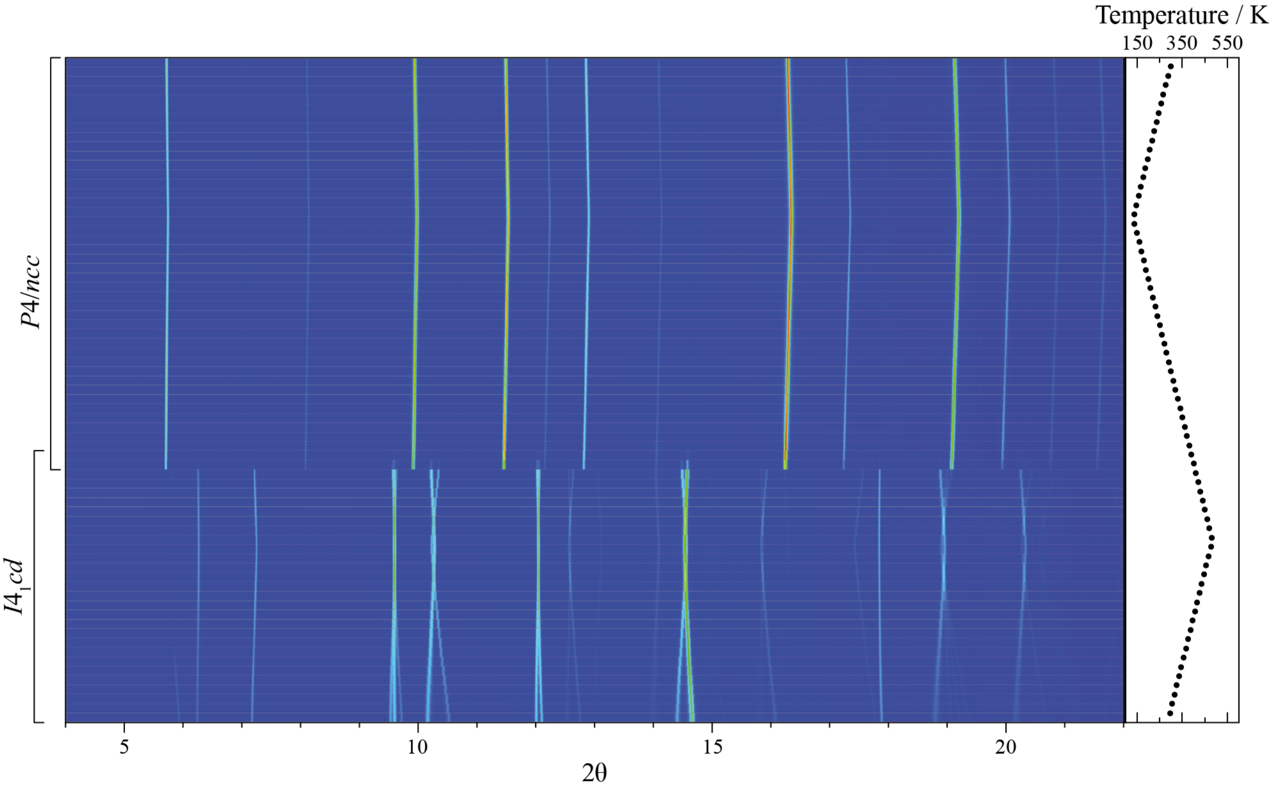

Figure S4: Variable temperature powder diffraction patterns of $[Bu_4N]Mn[Au(CN)_2]_3 \cdot [Bu_4N]ClO_4$ and its transformation product.

A Pawley refinement based on the $[Bu_4N]Ni[Au(CN)_2]_3$ $I4_1cd$ cell accounts for the majority of peaks present with unit cell parameters $a = 24.2890(3)$ Å, $c = 23.4744(4)$ Å, $V = 13848.8(4)$ Å^3 [Figure S6(b)]

Transformation into the ABX_3 phase leaves an equivalent of $[Bu_4N]ClO_4$ to be accounted for. It is not clear that this equivalent of $[Bu_4N]ClO_4$ is exsolved from the structure. The highest temperature reached in this experiment was 480 K, which is just below the melting point of $[Bu_4N]ClO_4$ (484–488 K)[S16] so we expect to see diffraction from this component at all temperatures. Just below 6 ° ($d \approx 10.5$ Å) is a peak which cannot be indexed on the tetragonal cell of **bcs**-$[Bu_4N]Ni[Au(CN)_2]_3$. On heating, this peak disappears from 440 K and reappears at 400 K on cooling.[2] This peak is at very similar d-spacing to the first, most intense peak of $[Bu_4N]ClO_4$[3] so we argue in the main text that it likely arises from exsolved $[Bu_4N]ClO_4$, presumably present in a plastic phase [Figure S6(c)].

An alternative possibility we also flag here for completeness is that $[Bu_4N]ClO_4$ remains included within the structure of **bcs**-$[Bu_4N]Ni[Au(CN)_2]_3$. We note that the thermal expansion of the peak at $d \approx 10.5$ Å tracks that of the (00l) peaks in the main pattern, *e.g.* (004) at 10.5 ° / $d \approx$

---

[2] There is also a similar, weaker peak just below 12 °.

[3] The crystal structure of $[Bu_4N]ClO_4$ has not been reported.

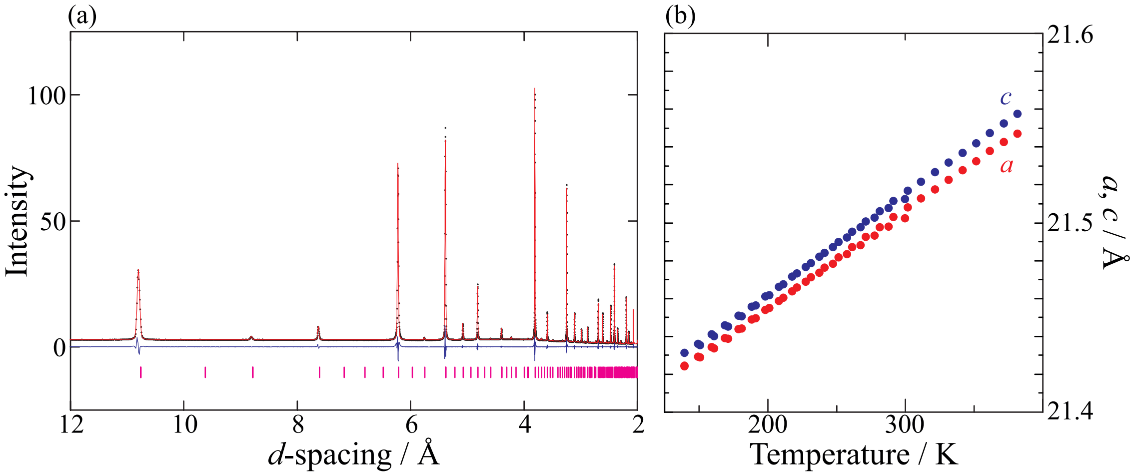

Figure S5: (a) Typical Pawley fit of $[\mathrm{Bu_4N}]\mathrm{Mn}[\mathrm{Au(CN)_2}]_3\cdot[\mathrm{Bu_4N}]\mathrm{ClO_4}$ in $P4/ncc$. $R_{\mathrm{wp}} = 4.203\%$, $R_{\mathrm{p}} = 2.536\%$, GoF $= 4.128$. (b) Variation in lattice parameters with temperature. All errors within markers.

5.9 Å. This peak, however, cannot be indexed on the parent cell metrics even in *P*1 symmetry. This means that—if $[\mathrm{Bu_4N}]\mathrm{ClO_4}$ is indeed included within **bcs**-$[\mathrm{Bu_4N}]\mathrm{Ni}[\mathrm{Au(CN)_2}]_3$—it would have to be present as a guest with a different periodicity to that of the main structure. Such behaviour has indeed been observed in other dicyanometallates (e.g. $\mathrm{Zn}[\mathrm{Ag(CN)_2}]_2\cdot\mathrm{AgCN}$[S14]). But, in the absence of further support for this interpretation, we feel the exsolution description given above is the more physically likely.

Table S2: Pawley refinement results for variable temperature powder diffraction of $[Bu_4N]Mn[Au(CN)_2]_3 \cdot [Bu_4N]ClO_4$.

Temperature / K	R_{wp}	R_{p}	GoF	a / Å	c / Å	Strain
299.8	4.20	2.54	4.13	21.5027(2)	21.5128(5)	0.0703(5)
288.1	4.37	2.63	4.29	21.4981(2)	21.5079(5)	0.0689(5)
277.8	4.53	2.73	4.47	21.4933(2)	21.5028(6)	0.0677(5)
267.6	4.62	2.78	4.56	21.4885(3)	21.4977(6)	0.0670(5)
257.6	4.69	2.82	4.62	21.4836(3)	21.4923(6)	0.0669(6)
247.5	4.74	2.86	4.66	21.4787(3)	21.4871(6)	0.0669(6)
237.6	4.74	2.84	4.63	21.4738(3)	21.4821(7)	0.0674(6)
227.7	4.67	2.79	4.61	21.4689(3)	21.4769(7)	0.0681(6)
218.0	4.58	2.73	4.51	21.4640(3)	21.4717(7)	0.0691(5)
208.1	4.50	2.68	4.42	21.4589(3)	21.4663(7)	0.0706(5)
198.3	4.39	2.62	4.31	21.4540(3)	21.4612(7)	0.0722(5)
188.6	4.24	2.54	4.19	21.4490(3)	21.4559(7)	0.0740(5)
178.7	4.13	2.47	4.07	21.4441(3)	21.4510(7)	0.0760(5)
168.9	4.03	2.41	3.97	21.4392(3)	21.4460(7)	0.0772(5)
159.2	3.90	2.34	3.83	21.4344(3)	21.4411(7)	0.0788(5)
149.4	3.77	2.27	3.72	21.4295(3)	21.4363(6)	0.0804(5)
139.6	3.70	2.22	3.65	21.4247(3)	21.4315(6)	0.0819(5)
139.7	3.90	2.34	3.85	21.4245(3)	21.4313(7)	0.0801(5)
150.9	4.03	2.41	3.99	21.4289(3)	21.4356(7)	0.0787(5)
161.1	4.14	2.47	4.10	21.4337(3)	21.4402(7)	0.0771(5)
171.2	4.27	2.55	4.21	21.4389(4)	21.4455(7)	0.0759(5)
181.3	4.35	2.59	4.28	21.4443(4)	21.4509(8)	0.0753(5)
191.3	4.42	2.64	4.34	21.4499(4)	21.4566(8)	0.0747(5)
201.3	4.54	2.69	4.49	21.4552(4)	21.4621(8)	0.0738(6)
211.4	4.66	2.77	4.60	21.4606(4)	21.4677(8)	0.0731(6)
221.4	4.79	2.86	4.72	21.466(4)	21.4733(8)	0.0724(6)
231.4	4.90	2.93	4.82	21.4713(4)	21.479(8)	0.0720(6)
241.5	4.97	2.97	4.92	21.4766(4)	21.4844(8)	0.0719(6)
251.5	5.01	2.97	4.94	21.4820(4)	21.4900(8)	0.0721(6)
261.5	5.05	2.99	4.97	21.4874(4)	21.4953(8)	0.0721(6)
271.5	5.05	3.01	4.96	21.4926(3)	21.5009(8)	0.0726(6)
281.6	5.00	2.99	4.90	21.4979(3)	21.5064(7)	0.0732(6)
291.6	4.97	2.97	4.90	21.5031(3)	21.5117(7)	0.0735(6)
301.8	4.93	2.95	4.86	21.5082(3)	21.517(7)	0.0728(6)
311.6	4.81	2.87	4.74	21.5130(3)	21.5219(7)	0.0728(6)
321.7	4.72	2.83	4.65	21.5178(3)	21.5268(7)	0.0724(6)
331.7	4.65	2.78	4.57	21.5227(3)	21.5318(6)	0.0716(6)
341.7	4.63	2.76	4.58	21.5278(3)	21.537(6)	0.0707(6)
351.7	4.62	2.76	4.56	21.5327(3)	21.5421(6)	0.0694(6)
361.7	4.60	2.73	4.54	21.5379(3)	21.5476(6)	0.0668(6)
371.9	4.56	2.68	4.49	21.5429(2)	21.5527(6)	0.0616(5)
381.6	4.87	2.92	4.79	21.5474(2)	21.5577(5)	0.0543(5)

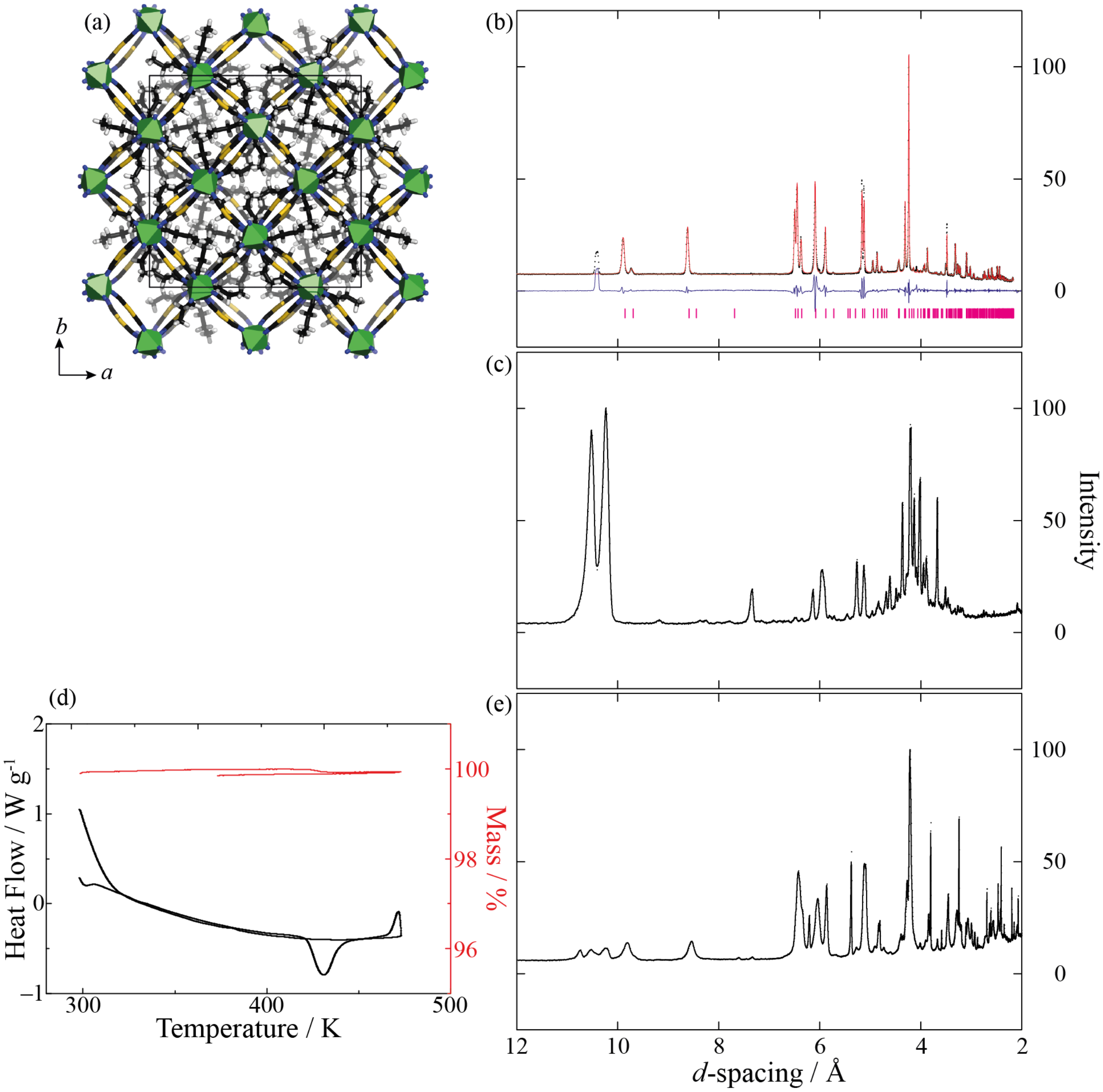

Figure S6: (a) Structure of [$\mathrm{Bu_4N}$]Ni[Au(CN)$_2$]$_3$ looking down c with 6-connected **bcs** topology. Channels down c are partially filled by the arms of [$\mathrm{Bu_4N}$]$^+$ (b) Pawley fit to powder diffraction pattern of **bcs**-[$\mathrm{Bu_4N}$]Mn[Au(CN)$_2$]$_3$ (**2**) in $I4_1cd$. The peak at $d \approx 10.5\,\text{Å}$ is attributed to [$\mathrm{Bu_4N}$]ClO$_4$. Lattice parameters: $a = 24.2890(3)\,\text{Å}$, $c = 23.4744(4)\,\text{Å}$, $V = 13848.8(4)\,\text{Å}^3$ $R_{\mathrm{wp}} = 6.103\%$, $R_{\mathrm{p}} = 3.521\%$, GoF $= 6.345$ (c) Powder diffraction pattern of [$\mathrm{Bu_4N}$]ClO$_4$. (d) DSC trace of [$\mathrm{Bu_4N}$]Mn[Au(CN)$_2$]$_3$·[$\mathrm{Bu_4N}$]ClO$_4$ (e) Powder diffraction pattern of sample recovered from DSC. The three peaks below 10 Å imply that a mixture of (**2**) and exsolved [$\mathrm{Bu_4N}$]ClO$_4$ is present.

4 Calorimetry and Gravimetry

Methods

Differential Scanning Calorimetry (DSC) measurements with concurrent TGA was performed using a Mettler Toledo TGA/DSC 1 STARe System. Each sample was placed in an open alumina crucible and measurements performed under flowing dry N_2. Sample masses of between 20–50 mg were used to ensure a balance between signal amplitude and sharpness. Powders were finely ground and tamped with a Teflon rod to give a uniformly packed powder with a flat surface. As this instrument is not fitted with a cooling system there is a characteristic increase in heat flow from the sample on cooling due to the heat retained by the alumina crucible. Data were typically collected in the range 25-300 °C at 10 °C min^{-1}. This strategy was occasionally modified to perform a cycle at a lower temperature first or to go to a lower maximum temperature if the sample would decompose below 300 °C. Crucibles were cleaned between runs using 6 M HCl.

Discussion

The DSC data show one feature – a large, exothermic peak on heating with maximum at 430 K [Figure S6(d)]. This is 50 K higher than the temperature at which the variable-temperature diffraction changes. The powder diffraction pattern of the DSC sample recovered to room temperature [Figure S6(e)] looks similar to (b) but with additional peaks which are consistent with the positions of the most intense peaks of $[\text{Bu}_4\text{N}]\text{ClO}_4$. The origin interesting temperature disparity between transitions in DSC and diffraction data is unclear.

5 Magnetometry

Methods

Magnetic property measurements were carried out on using a Quantum Design MPMS-XL superconducting quantum interference device (SQUID). Microcrystalline samples were packed in gelatine capsules and inserted securely into diamagnetic plastic straws. Direct current (DC) magnetisation was measured for all samples on warming from 2 K to 300 K under an applied DC field of 100 Oe. All samples were first measured after having been cooled in zero field and then cooled in an applied DC field of 100 Oe.

Discussion

Magnetometry data for (**1**) in the range 2–300 K are shown in Figure S7. The effective magnetic moment, μ_{eff}, and Curie temperature, θ_{C}, were extracted from linear fits to the inverse susceptibility data. (**1**) is paramagnetic with magnetic moment and Curie temperature of 4.70 μ_{B} / -0.09 K. The magnitude of the magnetic moment is quite small for high-spin *d*^{5} but also much higher than the spin-only, or Russell-Saunders coupling values for low-spin *d*^{5} ($= 1.73\,\mu_{\text{B}}$ and $= 2.24\,\mu_{\text{B}}$).[S17] The observed value would be consistent with a mixture of high-spin and low-spin Mn^{2+}. This is similar to the value of 4.53 μ_{B} reported for KMn(CN)$_3$ where half the Mn^{2+} is N-bound, hence high-spin, and half C-bound, hence low spin.[S18] Understanding the magnetic behaviour of (**1**) will require further work as the data do not immediately appear consistent with the crystallographic model. The possibility of the presence of small quantities of impurities should not be excluded.

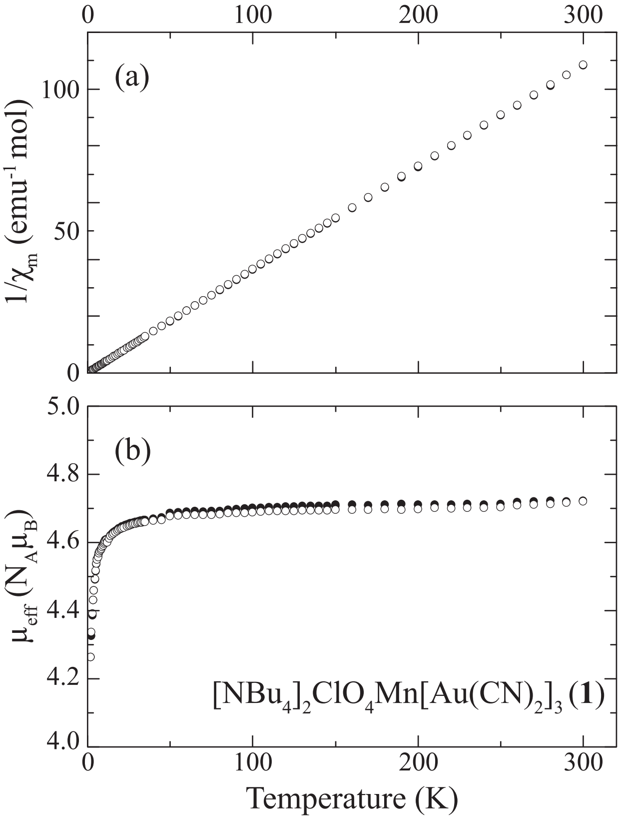

Figure S7: Magnetometry for **1**. Inverse susceptibility vs. temperature (a) and moment vs. temperature (b) show little, if any, interaction between magnetic sites. The moment is not consistent with isolated d^5 high-spin ions (**6**).[S19] Zero-field-cooled is shown as hollow circles and field-cooled as filled circles.

6 References

(S1) Hill, J. A. Structural chemistry of transition metal dicyanometallates. Ph.D. thesis, Department of Chemistry, University of Oxford, 2016.

(S2) Cosier, J.; Glazer, A. M. *J. Appl. Crystallogr.*, **1986**, *19*, 105–107.

(S3) *CrysalisPro*; Rigaku Oxford Diffraction, 2015.

(S4) Nowell, H.; Barnett, S. A.; Christensen, K. E.; Teat, S. J.; Allan, D. R. *J. Synchrotron Radiat.*, **2012**, *19*, 435–441.

(S5) Goeta, A. E.; Thompson, L. K.; Sheppard, C. L.; Tandon, S. S.; Lehmann, C. W.; Cosier, J.; Webster, C.; Howard, J. A. K. *Acta Crystallogr. Sect. C*, **1999**, *55*, 1243–1246.

(S6) Betteridge, P. W.; Carruthers, J. R.; Cooper, R. I.; Prout, K.; Watkin, D. J. *J. Appl. Crystallogr.*, **2003**, *36*, 1487–1487.

(S7) Parois, P.; Cooper, R. I.; Thompson, A. L. *Chem. Cent. J.*, **2015**, *9*, 30.

(S8) Cooper, R. I.; Thompson, A. L.; Watkin, D. J. *J. Appl. Crystallogr.*, **2010**, *43*, 1100–1107.

(S9) Spek, A. L. *J. Appl. Crystallogr.*, **2003**, *36*, 7–13.

(S10) van der Sluis, P.; Spek, A. L. *Acta Crystallogr. Sect. A*, **1990**, *46*, 194–201.

(S11) Coelho, A. A. *TOPAS-Academic, V4.1*, **2007**, Coelho Software.

(S12) Lefebvre, J.; Chartrand, D.; Leznoff, D. B. *Polyhedron*, **2007**, *26*, 2189–2199.

(S13) Hill, J. A.; Thompson, A. L.; Goodwin, A. L. *J. Am. Chem. Soc.*, **2016**, *138*, 5886–5896.

(S14) Goodwin, A. L.; Kennedy, B. J.; Kepert, C. J. *J. Am. Chem. Soc.*, **2009**, *131*, 6334–6335.

(S15) Hoskins, B. F.; Robson, R.; Scarlett, N. V. Y. *Angew. Chem. Int. Ed. Engl.*, **1995**, *34*, 1203–1204.

(S16) Hervert, K. L. *Encyclopedia of Reagents for Organic Synthesis*; John Wiley & Sons, Ltd: London, UK, 2001.

(S17) Entley, W. R.; Girolami, G. S. *Inorg. Chem.*, **1994**, *33*, 5165–5166.

(S18) Qureshi, A. M.; Sharpe, A. G. *J. Inorg. Nucl. Chem.*, **1968**, *30*, 2269–2270.

(S19) Goldenberg, N. *Trans. Faraday Soc.*, **1940**, *36*, 847–854.